

Noise Reduction from Vertical-Component Seismograms Recorded by Broadband Ocean-Bottom Seismometers Deployed at the Western Pacific

Yuki Kawano¹ , Takehi Isse^{*1} , Hitoshi Kawakatsu^{1,2} , Hajime Shiobara¹ , Nozomu Takeuchi¹ , Hiroko Sugioka³ , YoungHee Kim⁴ , Hisashi Utada¹ , and Sang-Mook Lee⁴ 

ABSTRACT

We modified existing methods of noise reduction to data recorded by Japanese broadband ocean-bottom seismometers (BBOBSs) deployed on the western Pacific seafloor conducted as the Oldest-1 Array observation. We removed the tilt and compliance noise that are dominant in low-frequency seismograms. We estimated the noise transfer function from the horizontal- to vertical-component seismograms to remove tilt noise from the vertical component. Throughout the observation period of about one year, the tilt noise transfer function was time-invariant and in phase at low frequencies (< 0.06 Hz), which, in contrast to previous studies, enabled us to apply a constant transfer function and to estimate the tilt of the sensor. We estimated the noise transfer function from the pressure- to the vertical-component records and removed the compliance noise in the frequency range of 0.002–0.02 Hz. As a result of tilt and compliance noise removal, noise levels were reduced by up to 20 dB at frequencies below 0.03 Hz. We show that tilt noise reduction using the constant transfer function is appropriate for Japanese BBOBSs equipped with the CMG-3T sensor. Tilt angles of Oldest-1 Array are estimated as 0.3°–1.1° and maximum tilt directions are along the H1 component of the sensor, which are attributed to the architecture of the CMG-3T sensor.

KEY POINTS

- We modified existing tilt and compliance noise reduction algorithms for Japanese broadband ocean-bottom seismometer (BBOBS).
- Using this method, we achieved noise reduction up to 20 dB at frequencies below 0.03 Hz.
- Unlike some previous studies, the noise transfer function did not vary over a one-year deployment.

Supplemental Material

INTRODUCTION

Innovations in ocean-bottom seismometers (OBSs) have allowed us to obtain long-term, broadband seismic data on the seafloor (e.g., [Beauduin and Montagner, 1996](#); [Kanazawa et al., 2001](#); [Webb et al., 2001](#); [Suetsugu and Shiobara, 2014](#)). Long-term seafloor observation of OBSs provides critical observations for the deep seismic structures of the Earth. However, the analysis of low-frequency data recorded by OBS has been more challenging than that of land data, owing to the high noise level originating from the seafloor.

There are two types of noise originating from seafloor current and seafloor pressure perturbation: tilt noise and compliance noise. Tilt noise depends on the accuracy of the sensor's leveling, with more precisely leveled sensors showing lower tilt noise levels. Because it is difficult to align the vertical axis of the sensor of the OBS in the gravitational direction exactly, a deviation (θ) remains. Hence, noisy horizontal-component records can be projected onto vertical-component seismograms ([Crawford and](#)

1. Earthquake Research Institute, The University of Tokyo, Tokyo, Japan,  <https://orcid.org/0000-0002-5178-3645> (YK);  <https://orcid.org/0000-9087-8711> (TI);  <https://orcid.org/0000-0001-9161-5024> (HK);  <https://orcid.org/0000-0002-3319-6383> (HS);  <https://orcid.org/0000-0003-3636-7800> (NT);  <https://orcid.org/0000-0001-5885-5675> (HU); 2. Institute of Earth Sciences, Academia Sinica, Taipei, Taiwan; 3. Graduate School of Science, Kobe University, Kobe, Hyogo, Japan,  <https://orcid.org/0000-0003-1883-4049> (HS); 4. School of Earth and Environmental Sciences, Seoul National University, Seoul, Republic of Korea,  <https://orcid.org/0000-0002-1111-632X> (YHK);  <https://orcid.org/0000-0002-8032-0316> (S-ML)

*Corresponding author: tisse@eri.u-tokyo.ac.jp

Cite this article as Kawano, Y., T. Isse, H. Kawakatsu, H. Shiobara, N. Takeuchi, H. Sugioka, Y. H. Kim, H. Utada, and S.-M. Lee (2023). Noise Reduction from Vertical-Component Seismograms Recorded by Broadband Ocean-Bottom Seismometers Deployed at the Western Pacific, *Bull. Seismol. Soc. Am.* **XX**, 1–13, doi: [10.1785/0120220256](https://doi.org/10.1785/0120220256)

© Seismological Society of America

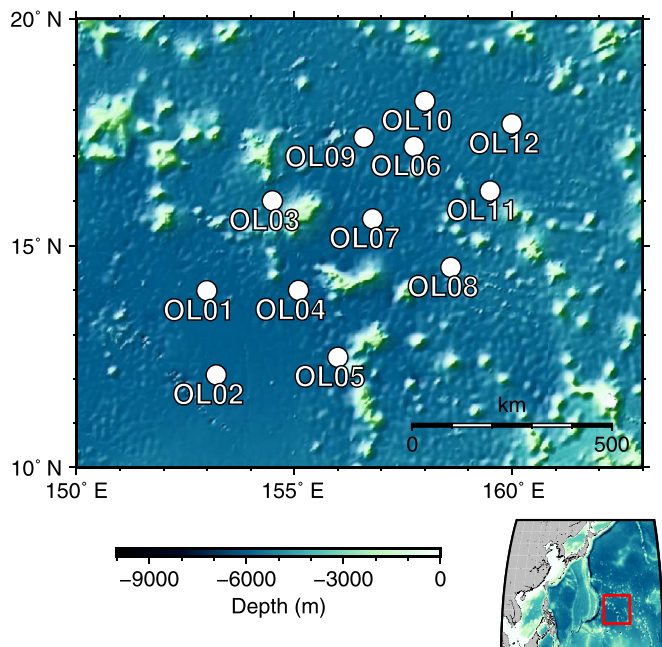


Figure 1. Station location of the Oldest-1 Array. The white filled circles represent the locations of broadband ocean-bottom seismometers (BBOBSs) with the station names labeled. The area plotted is indicated as the red box in the inset map on the right bottom. The color version of this figure is available only in the electronic edition.

Webb, 2000). Compliance noise originates from long-period seafloor deformation under seafloor pressure perturbation caused by long-period ocean surface gravity waves (infragravity waves) that have longer periods than wind-driven waves and swells (e.g., Crawford *et al.*, 1991). These noises are unique to each station, because the deformation response depends on the accuracy of leveling and structure beneath a particular station.

Many attempts have been made to reduce low-frequency noise in OBS data (Crawford and Webb, 2000; Bell *et al.*, 2015; Lin *et al.*, 2016; Deen *et al.*, 2017; Tian and Ritzwoller, 2017; Janiszewski *et al.*, 2019; Yang *et al.*, 2020). In particular, Crawford and Webb (2000) developed a method to reduce low-frequency noise in vertical-component seismograms and achieved up to 25 dB noise reduction. They further compared the noise level of the vertical-component seismograms recorded by a seismometer leveled within $\theta = 0.2^\circ$ to a nearby well-leveled ($\theta = 0.006^\circ$) gravimeter and found that the low-frequency noise level of the gravimeter is up to 20 dB lower than that of the seismometer. Bell *et al.* (2015) removed tilt and compliance noise from the vertical-component seismograms recorded by the Cascadia initiative and showed that the estimated θ was in the range of 0.1° – 1.5° . Deen *et al.* (2017) demonstrated the effectiveness of the noise reduction method at a lower frequency range by observing the Earth's hum in noise-reduced vertical-component seismograms collected in the Indian Ocean.

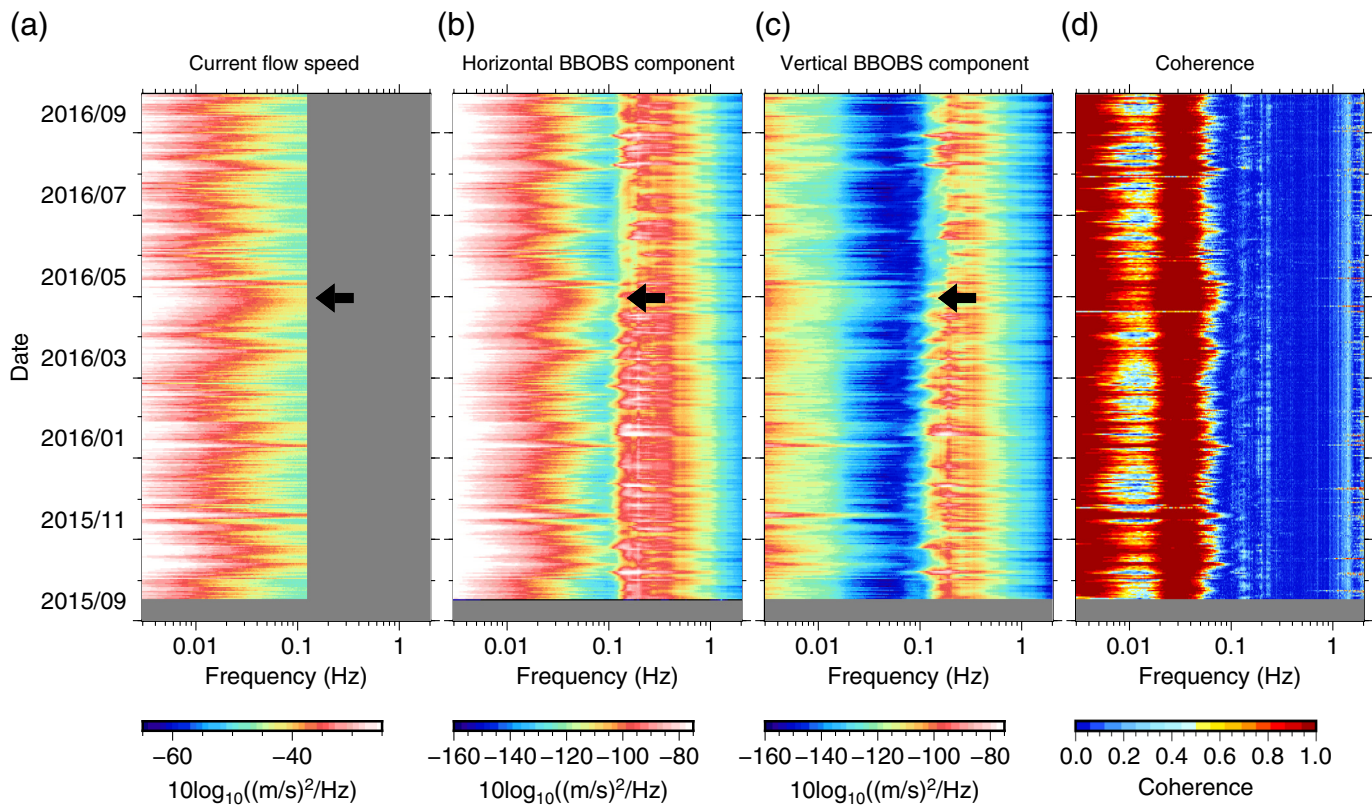
Although noise reduction methods have been established for instruments made in the United States and Europe, there have been no attempts to adapt a method specific to the broadband OBS (BBOBS) developed in Japan, particularly for BBOBSs developed by the Earthquake Research Institute (ERI-BBOBSs), because the ERI-BBOBSs have provided data with high signal-to-noise ratios (SNRs). The design of ERI-BBOBS differs from that of other BBOBS. All necessary components, including batteries, recorders, and seismic sensors (CMG-3T with a flat frequency range between 0.0028 and 50 Hz), are installed in a titanium alloy sphere housing 650 mm in diameter attached to an anchor (Suetsugu and Shiobara, 2014; Shiobara *et al.*, 2021). This heavy but compact design facilitates coupling between BBOBS and sediments and lowers the center of mass of the BBOBS, leading to a higher resistance to the seafloor current.

In this study, we used seismograms recorded in the seafloor array (Oldest-1 Array) with ERI-BBOBSs on the oldest Pacific basin (Fig. 1; Table S1, available in the supplemental material to this article) to design a method for noise reduction. The oldest Pacific basin is an ideal place to design and test the method because it is away from major tectonic structures, reducing the low-frequency noise. The Oldest-1 Array, located 1000 km east of Guam Island in the oldest Pacific Ocean at a seafloor depth of 5600–6000 m, is a collaborative Japanese–South Korean geophysical seafloor observation to study the oceanic lithosphere–asthenosphere system (Fig. 1; Table S1). In contrast to the United States and Europe, seafloor pressure measurement, which is necessary to remove the compliance noise, has not been standardized for ERI-BBOBSs. This deployment was the first to use ERI-BBOBSs equipped with a differential pressure gauge (Araki and Sugioka, 2009) at all 12 stations.

In this article, we first summarize the low-frequency noise typically observed on the BBOBSs and then describe a noise reduction method developed based on Crawford and Webb (2000) and Bell *et al.* (2015), which we modified to better suit data recorded by ERI-BBOBSs. Because of the malfunction of one ERI-BBOBS (OL12), we applied noise reduction to 11 ERI-BBOBSs. We then demonstrate the effectiveness of the proposed method by showing noise-reduced spectra and seismograms and discuss the tilt of the sensors.

LOW-FREQUENCY NOISE ON ERI-BBOBS

Tilt noise is generated by the seafloor current that flows past the instrument (Crawford and Webb, 2000) and is significant in horizontal-component seismograms. The time variation of the horizontal noise recorded by an ERI-BBOBS is consistent with that of the current flow speed (e.g., Shiobara *et al.*, 2013). Figure 2 compares the daily power spectral densities of the horizontal current flow speed measured by an ocean-bottom electromagnetic current profiler that measures the speed and direction of horizontal flow, and horizontal- and vertical-component seismograms recorded by an ERI-BBOBS



deployed offshore at Miyagi, Japan, at a seafloor depth of 3400 m, with two sensors separated by approximately 300 m (Fig. S1). This observation was performed to observe the frontal bores at the Japan trench, as discovered by Fukao *et al.* (2016). The time variations of the horizontal-component seismograms correlate with those of the current flow speed (e.g., black arrows in Fig. 2a,b), suggesting that the seafloor current is the dominant noise source for the horizontal-component seismograms at a frequency lower than 0.1 Hz.

The tilt noise is also observable in vertical-component seismograms, showing a coherent time variation with the current flow speed (e.g., black arrows in Fig. 2a,c) but with much lower noise levels than the horizontal component (Fig. 2b,c). The daily coherence between the horizontal and vertical components (see Appendix for the detailed methodology) is approximately one at frequencies below 0.07 Hz (Fig. 2d). When the seafloor current was strong with frequencies up to 0.1 Hz, the coherence also becomes high at higher frequencies (Fig. 2a,d), suggesting that the dominant cause of the coherence is tilt noise. This study provides the first direct evidence of correlation between horizontal seafloor current and the tilt noise. The lower coherence in the frequency range of 0.01–0.02 Hz is due to the influence of compliance noise.

Figure 3a shows the temporal variations in the flow direction of the seafloor current. The daily average flow direction fluctuated at 90°–180°. The data sampled at one-minute intervals reveal that the current flow fluctuates throughout the day. The one-year average value of the flow direction is

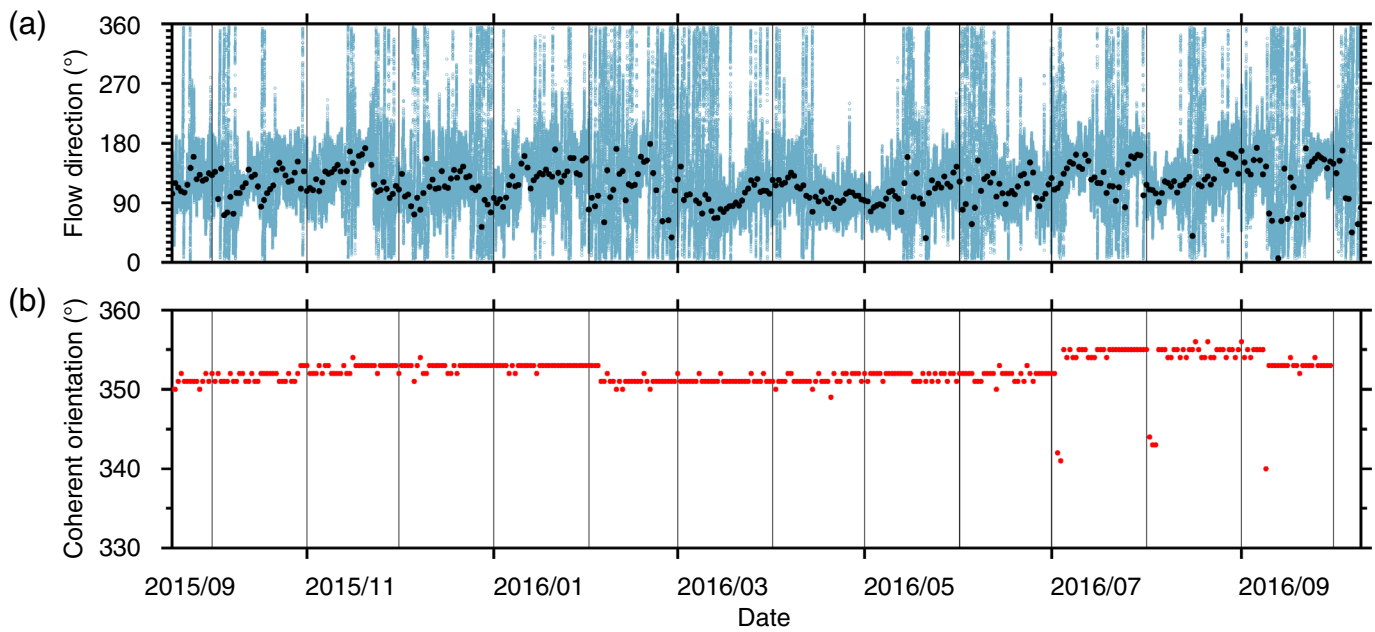
Figure 2. Power spectral density (PSD) as a function of time and frequency recorded at offshore Miyagi (Fig. S1). The vertical axis indicates the year and month (yyyy/mm) of observations. The daily PSD is calculated as follows: the 24 hr time series is first divided into 2000 s sections with a 50% overlap between adjacent sections. Then, a median value of power at each frequency is obtained from the PSD of each section. PSD obtained from (a) current flow speed, (b) horizontal-component BBOBS data, (c) vertical-component BBOBS data, and (d) squared coherence between the horizontal- and vertical-component BBOBS data are shown. The horizontal component is taken along the direction that maximizes the squared coherence between the horizontal and vertical components at a frequency range of 0.02–0.06 Hz. There are no data for the gray-shaded area due to sampling rate or observation period. The black arrows indicate an example of coherent relationships among panels (a)–(c). The value beyond the range of each color scale is saturated in panels (a)–(c). The color version of this figure is available only in the electronic edition.

approximately N118°E, indicating that the seafloor current flows in the direction along the slope of the Japan trench (Fig. S1). In contrast, the maximum coherent orientation (see Appendix) that corrected to the angle from the north is stable and points to approximately N352°E (Fig. 3b), which is significantly different from the flow direction (Fig. S1).

METHODS

Calculation of the daily tilt noise transfer function

Following previous studies (Crawford and Webb, 2000; Bell *et al.*, 2015), we calculated the tilt noise transfer function from the horizontal- to the vertical-component seismograms



(H-to-Z transfer function) from coherence of the seismograms. Using the daily cross and power spectra of noise (see Appendix), we obtain the H-to-Z transfer function of day d , $D_d(f)$, as

$$D_d(f) = \frac{G_{HZ}(f)}{G_{HH}(f)}, \quad (1)$$

$$A_d(f) = \frac{|G_{HZ}(f)|}{G_{HH}(f)}, \quad (2)$$

$$\phi_d(f) = \arctan \left[\frac{\text{Im}(G_{HZ}(f))}{\text{Re}(G_{HZ}(f))} \right], \quad (3)$$

in which $A_d(f)$ and $\phi_d(f)$ are the admittance and phase of the H-to-Z transfer function, respectively. We estimated the maximum coherence orientation (see Appendix). The horizontal component for the estimation of the daily transfer function was estimated along the daily maximum coherent orientation. Figure 4 shows an example of a daily H-to-Z transfer function. The squared coherence is nearly one at frequencies lower than 0.04 Hz (Fig. 4a). It drops at around 0.01 Hz because of the presence of the compliance noise that affects the tilt noise. The squared coherence is small at frequencies higher than approximately 0.05 Hz because of microseisms. At frequencies lower than 0.04 Hz in which coherence is high (>0.96), both admittance and phase of the transfer function are stable and have almost no frequency dependence. The admittance is $\sim 0.020 \pm 0.0004$. The phase is nearly zero ($<5^\circ$; Fig. 4b,c), indicating that the horizontal- and vertical-component seismograms are in phase.

Figure 3. (a) Time variation of the flow direction of the seafloor current at offshore Miyagi. The light blue circles are data sampled at the one-minute interval and the black dots are the one-day average of the blue circles. The direction is measured clockwise from the north. The horizontal axis indicates the year and month (yyyy/mm) of observations. (b) Time variation of the observed coherent orientation that maximizes the squared coherence between the horizontal- and vertical-component seismograms. The coherent orientation here is measured from the north by correcting the H1 component direction of N12°E estimated using back azimuths of first arrival of large events. The color version of this figure is available only in the electronic edition.

Tilt noise removal procedure for the ERI–BBOBS

We measured daily H-to-Z transfer functions, which fluctuate in the lower coherent frequency range. However, both admittance and phase are stable during the observation periods at frequencies lower than 0.038 Hz, especially at 0.013–0.033 Hz in the higher coherent range (Fig. 5; and Fig. S3). The maximum coherent orientation is also stable during the observation (Fig. 6).

Bell *et al.* (2015) showed that both the maximum coherent orientation and the H-to-Z transfer function drifted systematically during the observation period and concluded that the H-to-Z transfer function should be estimated daily to account for those gradual changes. They estimated a frequency-dependent transfer function to account for the unknown mismatch in the response functions among different components. In contrast to previous studies, the maximum coherent orientations and H-to-Z transfer functions in this study are stable in amplitude and zero in phase throughout the observation period at frequencies with high coherence (Figs. 4–6). These characteristics are robust for the ERI–BBOBSs in various observation environments, such as the Oldest-1 Array (this study), the

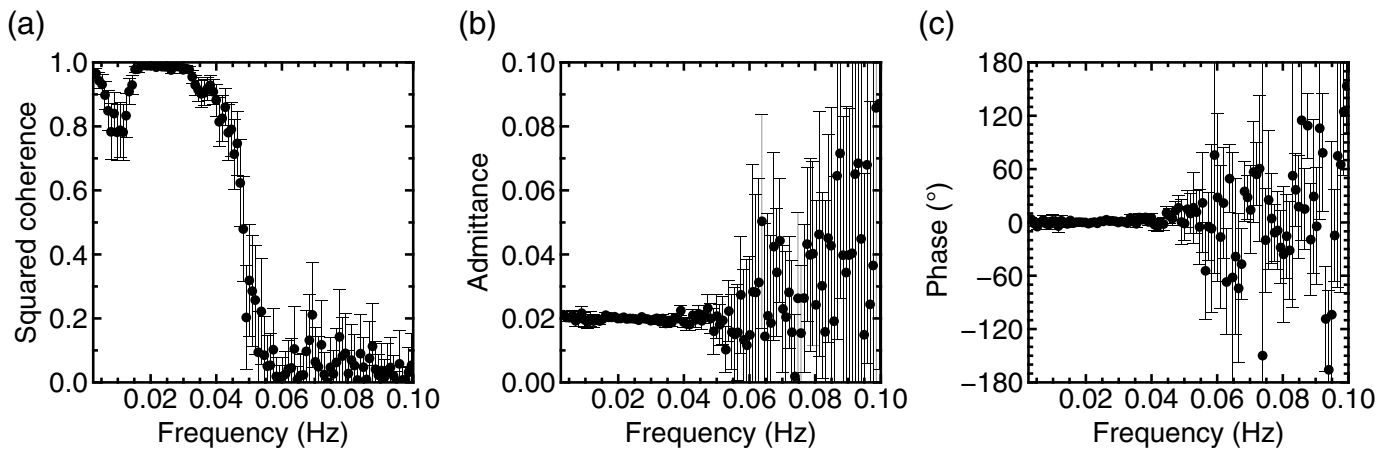


Figure 4. The squared coherence and the H-to-Z transfer function recorded at OL08 on 10 November 2018, showing typical data from Oldest-1 Array.

(a) Squared coherence. (b) Admittance. (c) Phase. Error bars represent a 95% confidence interval.

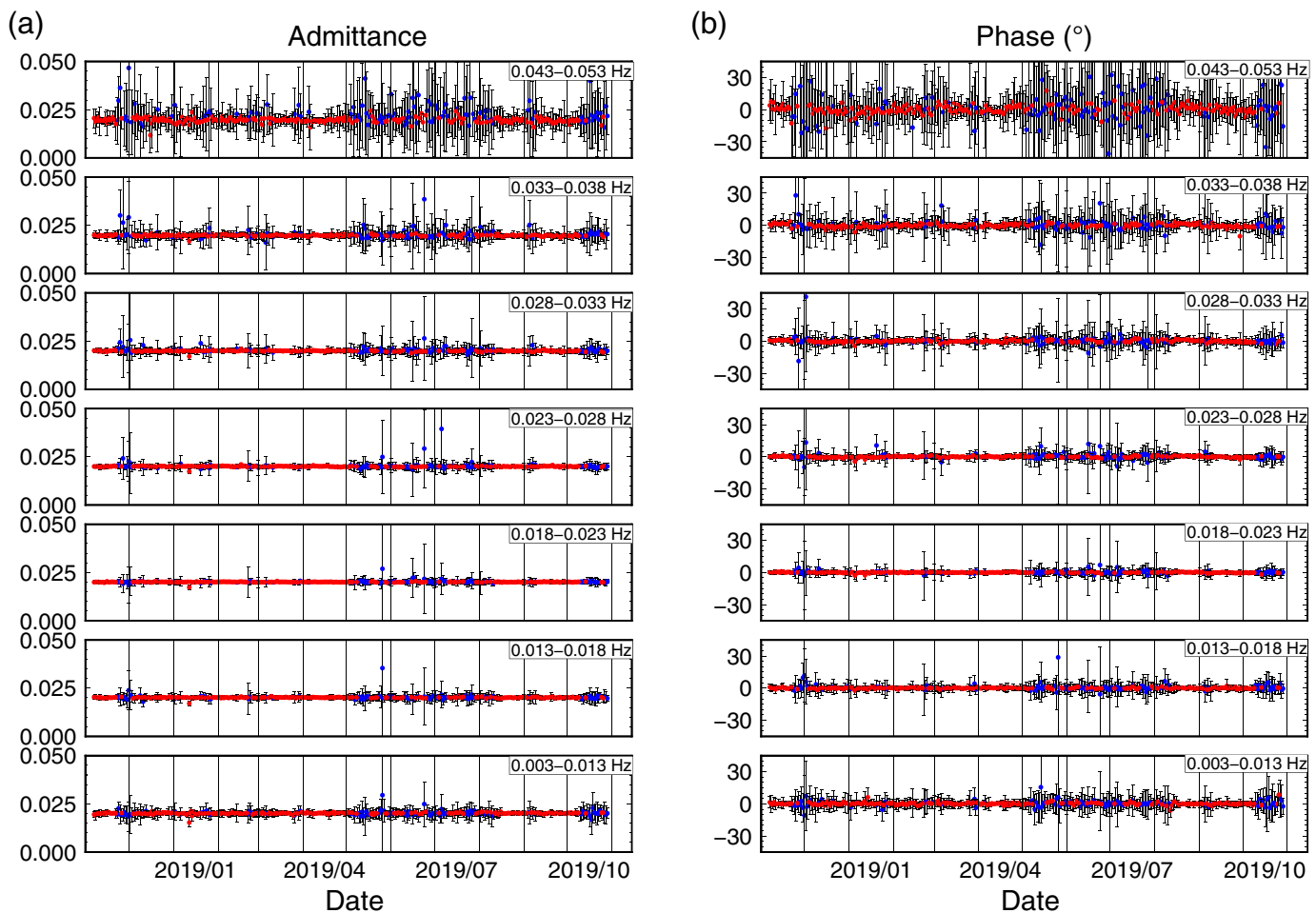


Figure 5. (a) The admittance of the noise transfer function between the horizontal- and vertical-component seismograms at station OL08. Each panel shows average values specific frequency band that is shown in each panel (upper right corner). The red and blue dots indicate the days for which squared coherence (averaged over a frequency range of 0.003–0.053 Hz) is

larger or less than 0.6, respectively. The error bars represent 95% confidence intervals. (b) Same as panel (a), but for the phase. Figure S3 shows the same figure without the red dots to avoid overlapping of red and blue dots. The color version of this figure is available only in the electronic edition.

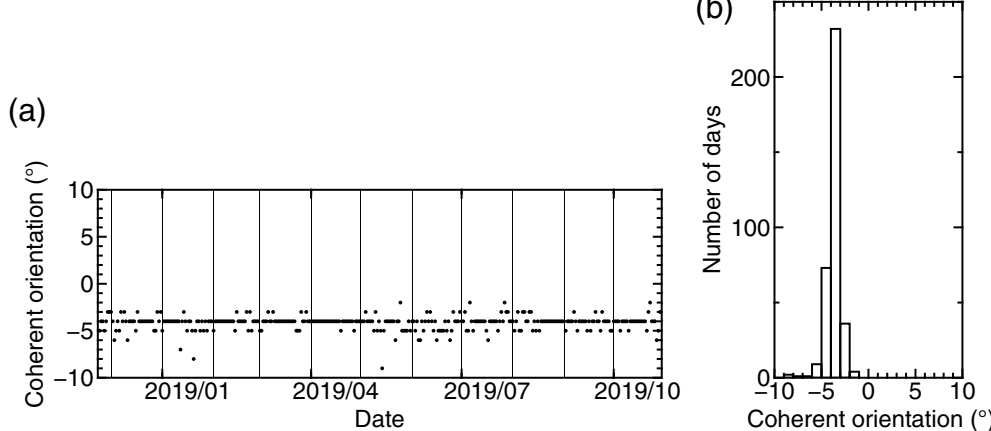


Figure 6. Estimated maximum coherent orientation of station OL08 that maximizes the squared coherence between the horizontal- and vertical-component seismograms, measured clockwise from the H1 component. (a) Time variation of the maximum coherent orientation. (b) A histogram of the coherent orientations in panel (a).

northwestern Pacific Ocean, and Ontong Java plateau (Isse et al., 2021). These observations suggest that a time- and frequency-invariant transfer function can be expressed as a tilt of the sensor in ERI-BBOBS. Therefore, we can apply tilt noise removal among all frequencies and observation periods once we estimate the transfer function.

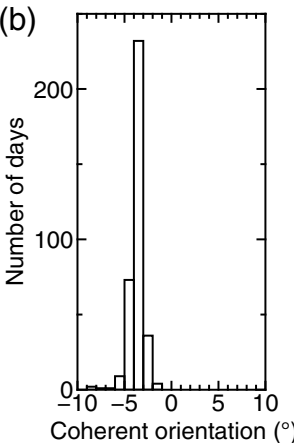
We extracted the most frequent value of the maximum coherent orientation during the observation period at each station (i) (Fig. 6b) and defined it as the representative maximum coherent orientation, α_i^{rep} . We then estimated a time-invariant admittance in the frequency range in which the uncertainty is small ($f = 0.018\text{--}0.023$ Hz; see Fig. 5 and Fig. S3). The representative admittance (A_i^{rep}) was obtained by averaging all daily calculated admittances in the frequency range of 0.018–0.023 Hz using only measurements with fractional uncertainties of 5% or less: $A_i^{\text{rep}} = \sum_d \sum_f A_d(f)/N$, in which N is the number of measurements. The tilt noise recorded on the vertical-component seismograms was estimated using the parameters (A_i^{rep} and α_i^{rep}). We proceed in the time domain in the following equation:

$$z_t(t) = z(t) - A_i^{\text{rep}} h(t), \quad (4)$$

in which $z_t(t)$ and $z(t)$ are the tilt noise-removed and observed vertical-component seismograms at a station i , respectively, and $h(t)$ is the horizontal-component record taken along the α_i^{rep} .

Compliance noise removal

The compliance noise in the tilt noise-removed vertical-component seismograms was subtracted in the same manner as that for the tilt noise removal. The transfer function between the vertical- and pressure-component signals (P-to-Z transfer



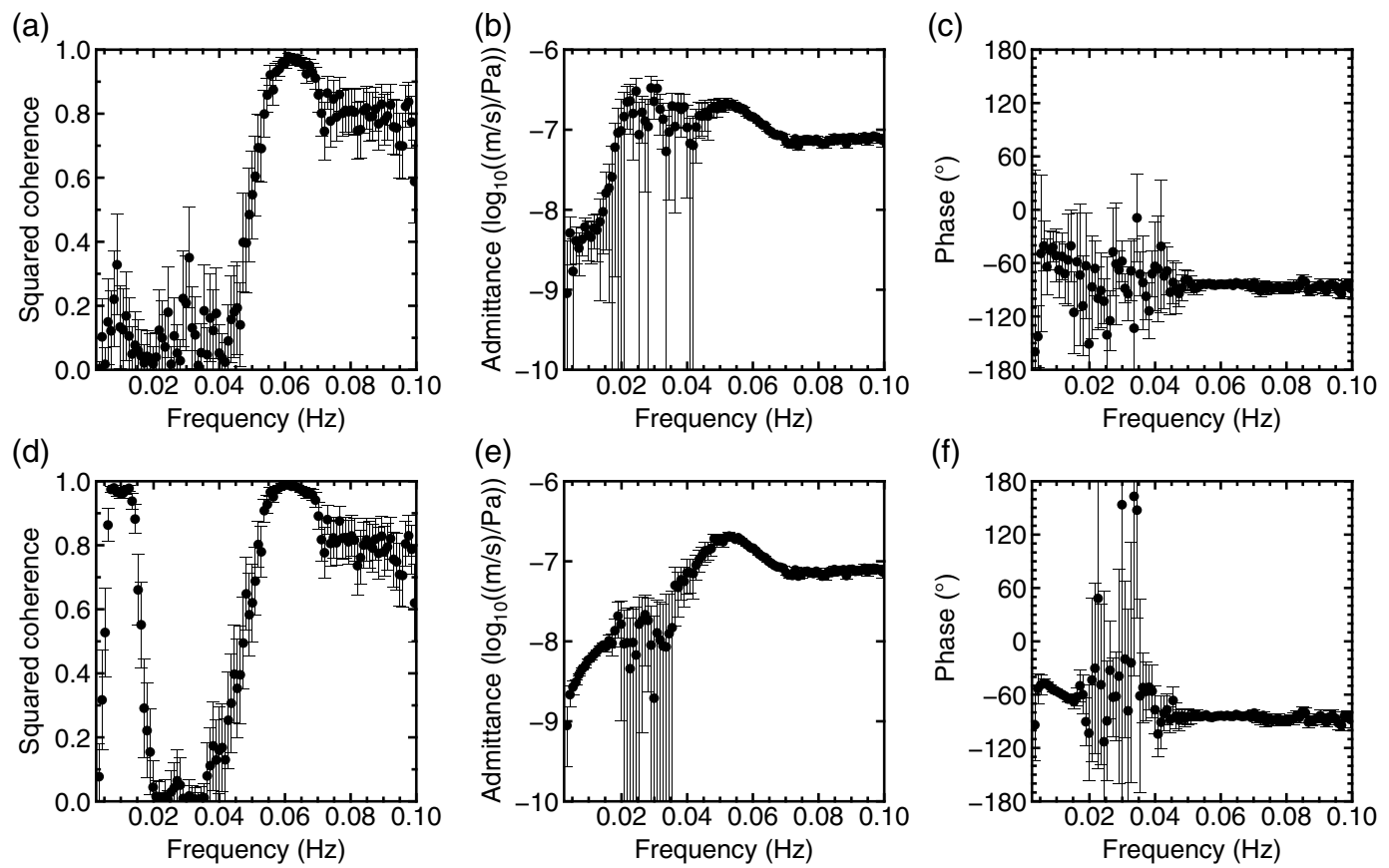
function), the seafloor compliance, depends on the shallow elastic structure. Thus, the seafloor compliance is time invariant but frequency dependent. We estimated a representative P-to-Z transfer function by averaging the daily calculated transfer functions over the observation period.

We calculated the daily P-to-Z transfer function and squared coherence using equations (A1–A4) in Appendix and equations (1–3). In these equations, horizontal-component seismograms (H) should be regarded as pressure-component records (P).

Figure 7 shows an example

of a daily P-to-Z transfer function using vertical-component seismograms before (Fig. 7a–c) and after (Fig. 7d–f) the tilt noise removal. The estimated transfer functions are similar in both cases, and the squared coherence is high at a frequency of 0.06 Hz or higher in which the vertical and horizontal components record the microseisms (Fig. S2). At a frequency of 0.02 Hz or lower, significant compliance noise is recorded on both records, resulting in broad peaks in the spectra at frequencies lower than ~0.02 Hz (Fig. S2). At these frequencies, the squared coherence between the vertical- and pressure-component records is significantly different (Fig. 7a,d): it is low (~0.2) when using seismograms before tilt noise removal, but it is high (~1) when using tilt noise-removed seismograms. In the latter case, both the admittance and phase show small uncertainties and are stable along the frequency. This suggests that the tilt noise is dominant in the vertical-component seismograms recorded by ERI-BBOBS and that tilt noise should be removed before the compliance noise removal method is applied. In this study, we choose 0.02 Hz as the maximum cutoff frequency of compliance noise for all stations because the coherence drops abruptly at that frequency (Fig. 7a), which is roughly the same (0.016–0.019 Hz) as that obtained from estimations using the seafloor depth of each station (Bell et al., 2015; Tian and Ritzwoller, 2017).

Figure 8 summarizes the process of estimating the representative P-to-Z transfer function using tilt noise-removed records. First, we obtain the daily P-to-Z transfer functions ($D_d(f)$) throughout the observation period (light pink dots in Fig. 8). Second, we extract admittances with fractional uncertainties that are smaller than 5% and phases with uncertainties that are smaller than 5° (red dots in Fig. 8) to estimate the time-invariant transfer function. If there are more than 30 extracted data points



at a frequency, we calculate a transfer function averaged over the data points at that frequency (open gray circles in Fig. 8): $A(f) = \sum_d^N A_d(f)/N$ and $\phi(f) = \sum_d^N \phi_d(f)/N$, in which d is the day and N is the number of days. Third, we fit the average P-to-Z transfer function ($A(f)$ and $\phi(f)$) using the cubic function and obtain the representative P-to-Z transfer function as $D_i^{\text{rep}}(f) = A_i^{\text{rep}}(f) \exp[\phi_i^{\text{rep}}(f)]$ at each station i .

Compliance noise removal is performed at a frequency range of 0.002–0.02 Hz in which compliance noise is observable (Fig. S2). We apply a cosine taper to the admittances at frequency ranges of 0.0018–0.002 Hz and 0.02–0.03 Hz to avoid abruptly cutting the frequency of noise reduction. In Figure 8, the representative P-to-Z transfer function applied to the cosine taper is shown by the dashed lines, and that in the 0.002–0.02 Hz is shown by the solid lines. At a frequency higher than 0.02 Hz, the representative admittance is estimated to be a few factors larger than the centroid of the daily calculated values. This difference would not distort seismograms significantly because (1) the cosine taper is applied to the admittance and the amplitude is suppressed and (2) the wavelength of water waves becomes short and does not reach the seafloor; thus, the amplitude of the compliance noise becomes small (Fig. S2).

We remove the compliance noise in the frequency domain as

$$Z_{tc}(f) = Z_t(f) - D_i^{\text{rep}}(f)P(f), \quad (5)$$

Figure 7. Same as Figure 4, but for the P-to-Z transfer function. Z-component data (a–c) before and (d–f) after the tilt noise removal are used in the calculation.

in which $Z_{tc}(f)$ is the Fourier transform of the tilt and compliance noise-removed vertical-component seismograms, $Z_t(f)$ is the Fourier transform of the tilt noise-removed vertical-component seismograms, and $P(f)$ is the Fourier transform of the pressure signal.

RESULTS: NOISE-REDUCED SPECTRA AND SEISMOGRAMS

At frequencies lower than ~0.04 Hz, there is a noticeable difference between the vertical-component noise spectra before and after the tilt noise removal (Fig. 9). The spectra after tilt noise removal are approximately 10–20 dB lower than before. The amount of noise reduction differed among the stations. The compliance noise peak is visible even in the noise spectra before the tilt and compliance noise removals in ERI-BBOBs, whereas the noise spectra of the U.S.-designed BBOBs equipped with a CMG-3T sensor shows a high noise level with no significant compliance noise peak before applying tilt noise removal (Janiszewski *et al.*, 2023). The compliance noise peak becomes more pronounced in the spectrum after tilt noise removal. The power of the compliance noise increases at a frequency of ~0.02 Hz, peaks at 0.009 Hz, and is overwhelmed by

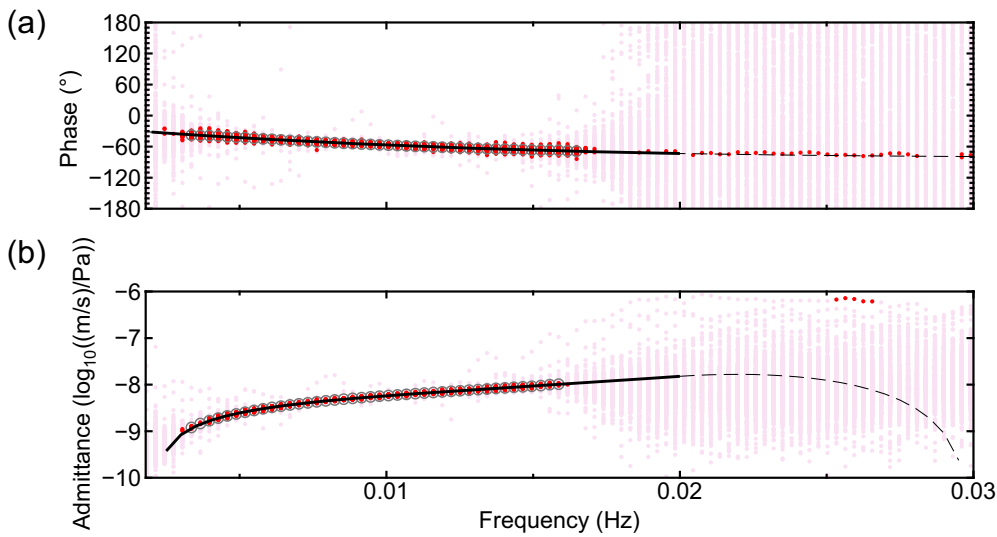


Figure 8. An example of the P-to-Z transfer function at OL08. (a) The phase of the P-to-Z transfer function. (b) The log of the admittance. The light-pink dots represent all daily P-to-Z transfer functions. The red dots represent the data points for which fractional uncertainties are smaller than 5% for admittances, or for which uncertainties are smaller than 5° for phases. The gray open circles represent the average transfer functions at that frequency. The solid black line is the fitted P-to-Z transfer function using cubic functions, and the dashed line indicates the transfer function we used in compliance noise reduction. The color version of this figure is available only in the electronic edition.

other background noise at 0.005 Hz or lower. After removing the compliance noise, the noise level was successfully reduced by 10–20 dB in the frequency range of 0.005–0.02 Hz.

Rayleigh waves in this frequency range are sensitive to the shear-wave velocity of the mantle low-velocity zone (LVZ), suggesting the importance of noise reduction in investigating the Lid and LVZ structure to understand the lithosphere–asthenosphere system. At frequencies higher than 0.1 Hz, the microseisms become dominant, and the energies of the tilt noise become relatively small; therefore, the vertical-component spectra before and after tilt noise removal do not exhibit any significant changes.

Figure 10 shows an example of noise-reduced Rayleigh wave signals band-pass filtered at 0.005–0.015 Hz. In the vertical records before both noise removals, it is difficult to recognize the propagation of the Rayleigh waves. In the tilt and compliance noise-removed records, the propagation of the fundamental-mode Rayleigh waves becomes very clear at about 1300 s after the event origin time. In addition, even the small-amplitude shear-wave propagation becomes recognizable approximately 980 s after the event origin time.

DISCUSSION

Tilt of the sensor and OBS

Crawford and Webb (2000) derived an equation for the seafloor current-induced acceleration for an OBS tilted by a small

angle from the gravitational direction. For frequencies lower than 0.1 Hz, the equation is approximately expressed in the following equations:

$$h \approx g \cos \theta \varepsilon, \quad (6)$$

$$v \approx -g \sin \theta \varepsilon - \frac{\varepsilon^2}{2} g \cos \theta, \quad (7)$$

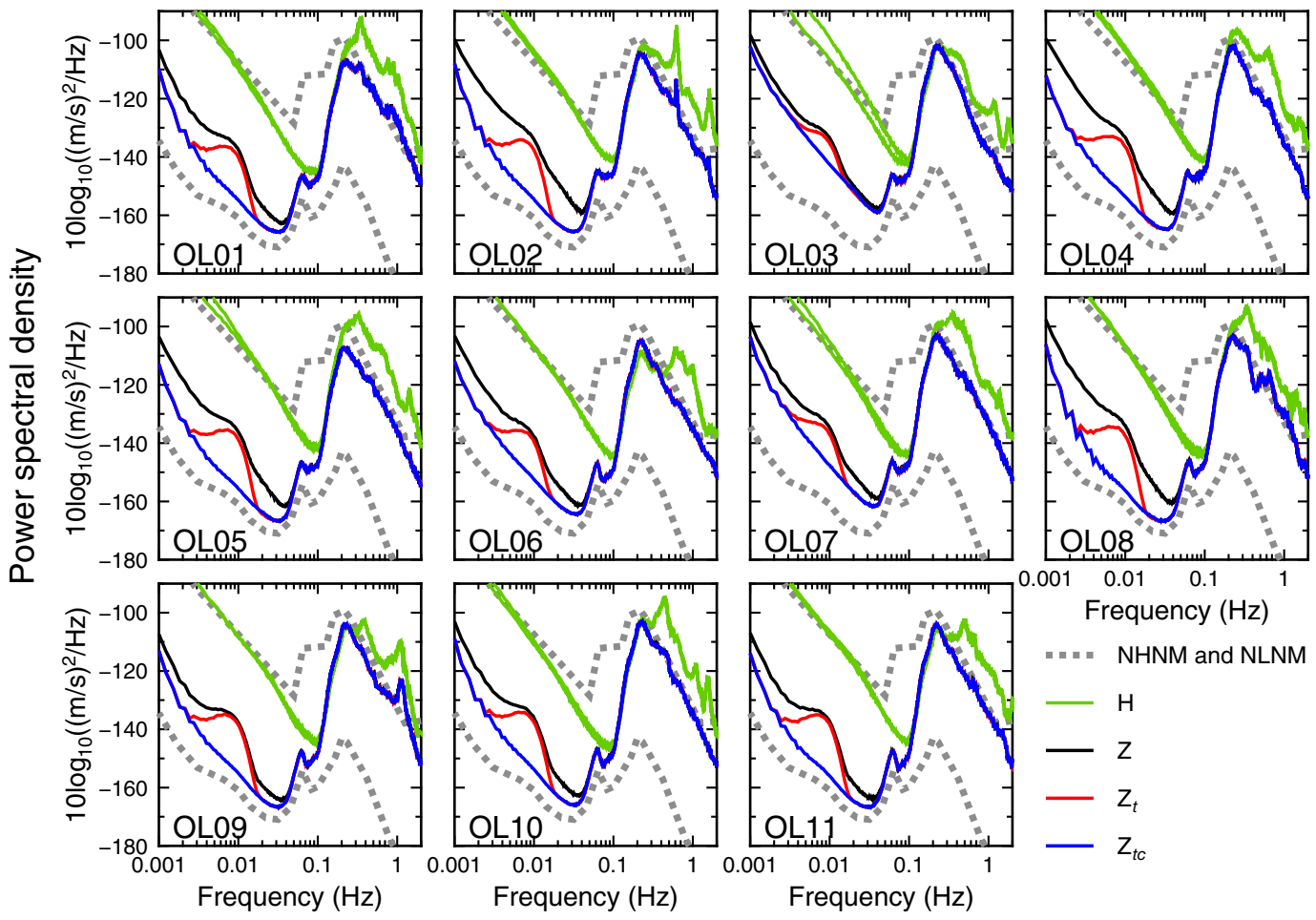
in which h and v are, respectively, the horizontal and the vertical components of the seismograph, which is tilted by an angle of θ , g is the gravitational constant, $\varepsilon(\omega,t)$ is a small frequency dependent rotation of the seismograph around the center of mass by seafloor current force, and $\theta, \varepsilon \ll 1$ is assumed.

When ground motions are present, we modify the equation to describe the total acceleration at low frequencies observed by the seismic sensor by adding a ground motion acceleration term:

$$\begin{cases} h \approx g \cos \theta \varepsilon + a_x(\omega,t) \cos \theta + a_z(\omega,t) \sin \theta \\ v \approx -g \sin \theta \varepsilon - \frac{\varepsilon^2}{2} g \cos \theta - a_x(\omega,t) \sin \theta + a_z(\omega,t) \cos \theta \\ = -\tan \theta h - \frac{\varepsilon^2}{2} g \cos \theta + \frac{a_z}{\cos \theta} \end{cases}, \quad (8)$$

in which $a_x(\omega,t)$ and $a_z(\omega,t)$ are the true horizontal and vertical ground-motion accelerations, respectively. If the second term of v is negligible, we can use $-\tan \theta$ as a transfer function and the estimated tilt noise-removed vertical data are proportional to $\frac{1}{\cos \theta}$ of the vertical ground acceleration. These equations require that the three components of the sensor always be orthogonal, even when the sensor is tilted. The seismometer based on the Galperin configuration known as “symmetric triaxial,” such as Streckeisen STS-2 or Nanometrics Trillium, satisfies this requirement.

On the other hand, the orthogonality of the CMG-3T (Guralp system, United Kingdom) seismometer used in the ERI-BBOBS depends on the leveling of the sensor. The CMG-3T seismometer (Usher *et al.*, 1978) consists of two horizontal sensor elements that are mutually orthogonal and one vertical. The vertical element is designed differently from the horizontal elements because of the presence of constant gravity acceleration; accordingly, the mass centering method of CMG-3T is different for the horizontal and vertical elements. Mass centering is performed on the horizontal component by tilting the base of the horizontal element. On the vertical element, the tension of the main spring was adjusted to change the force



without base movement. This difference in centering methods means that the tilt of the sensor is corrected for the horizontal elements but remains on the vertical element (Townsend, 2014). The observed horizontal components of the CMG-3T represent the true horizontal ground motions even when the sensor unit is tilted, whereas those of the Galperin-type seismometer are tilted. Therefore, equation (8) describing the case of the “symmetric triaxial” should be modified to

$$\begin{cases} h_{\text{cmg}} \approx g\varepsilon + a_x \\ v_{\text{cmg}} \approx -g \sin \theta \varepsilon - \frac{\varepsilon^2}{2} g \cos \theta - a_x \sin \theta + a_z \cos \theta \\ = -\sin \theta h_{\text{cmg}} - \frac{\varepsilon^2}{2} g \cos \theta + a_z \cos \theta \end{cases}, \quad (9)$$

in which h_{cmg} and v_{cmg} are the horizontal and vertical components of the CMG-3T, respectively. When the second term of v_{cmg} is negligible, we can use $-\sin \theta$ as a transfer function and the estimated tilt noise-removed vertical data are then proportional to $\cos \theta$ of the vertical ground acceleration.

It is not trivial to determine whether the second term of the vertical component is negligible ($\varepsilon \ll \theta$). Recent continuous tilt observation on the deep seafloor revealed that the tilt fluctuation of ERI-BBOBS was a few tens of microradians (Shiobara et al., 2021). The ERI-BBOBS checks and records the mass position output, which is the low-pass filtered (cut

Figure 9. Median noise power spectral densities for each station. The median from aggregate of the daily noise power spectral densities at each frequency is plotted. In each panel, the green line represents two horizontal-component spectra (H), the black line represents the no noise-removed (Z), the red line represents the tilt noise-removed (Z_t), and the blue line represents the tilt and compliance noise-removed vertical-component spectrum (Z_{tc}). The gray dashed lines are the new high-noise model (NHNM) and new low-noise model (NLNM) (Peterson, 1993). The color version of this figure is available only in the electronic edition.

off at a period of 360 s of the eigen period) acceleration data; once a day, the mass centering operation starts when the tilt of the sensor exceeds approximately $\pm 10\mu$ rad ($\pm 6 \times 10^{-4}\circ$), recording the mass position output before and after the operation. We estimated the tilt fluctuation of the sensor from the horizontal mass position output. The estimated tilt fluctuation is much smaller than the mass centering threshold, which is sufficiently small for the second term in equation (9) to be neglected (Fig. 11a). Correcting the mass centering operation effect, we obtained the cumulative tilt change along two horizontal components of the OBS itself (Fig. 11b). The tilt change data suggest that a rapid tilt change ($\sim 0.01^\circ$) caused by sinking of the OBS into the mud occurs during the first several days of the observation until it becomes stable, and that the following

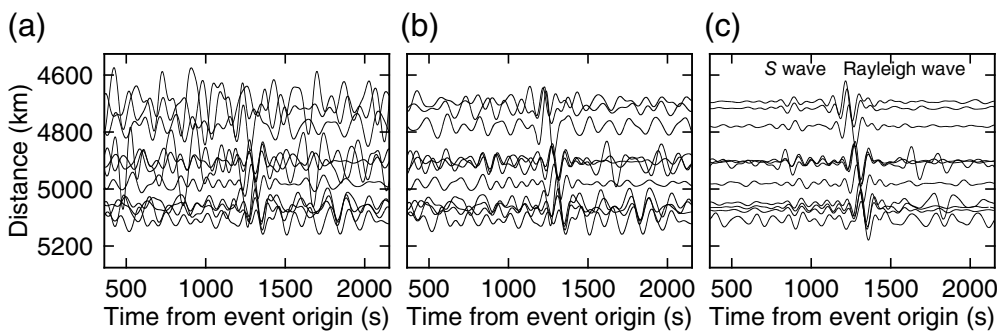


Figure 10. An example of Rayleigh-wave propagation in noise-reduced records at the Oldest-1 Array. (a) The no noise-reduced, (b) tilt noise-reduced, and (c) tilt and compliance noise-reduced vertical-component seismograms, respectively. Each waveform is band-pass filtered from 0.005 to 0.015 Hz. The seismic event that occurred in Tonga Island at 9:01:12.6 GMT on 5 August 2019 with a moment magnitude of 5.7 and a focal depth of 12 km is used.

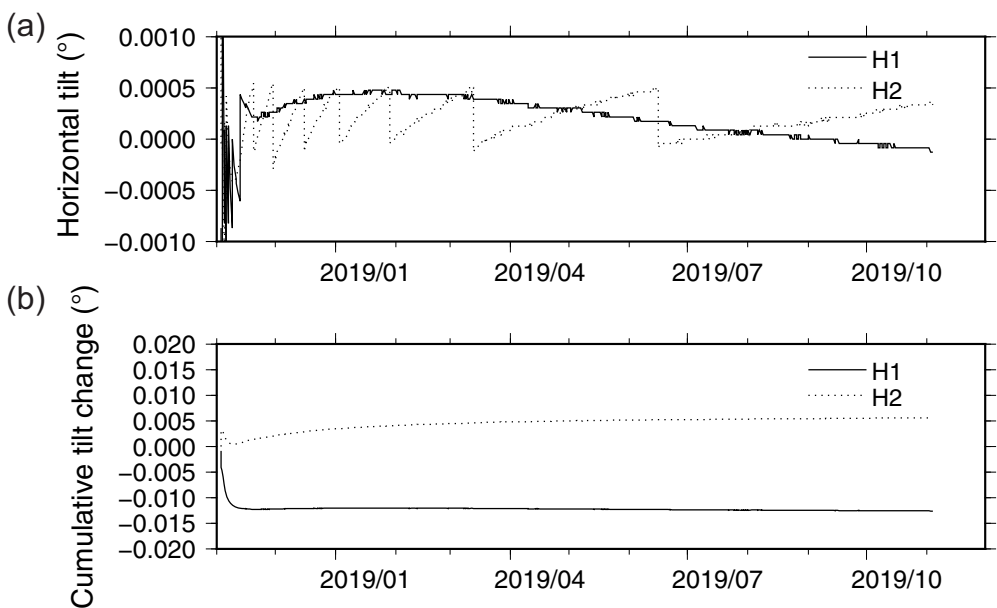


Figure 11. (a) Horizontal tilt angles estimated from the mass position output signals of H1 (north-south) and H2 (east-west) component of the sensor of the station OL06. (b) Cumulative tilt change along each horizontal component of OL06 obtained by correcting mass centering effect.

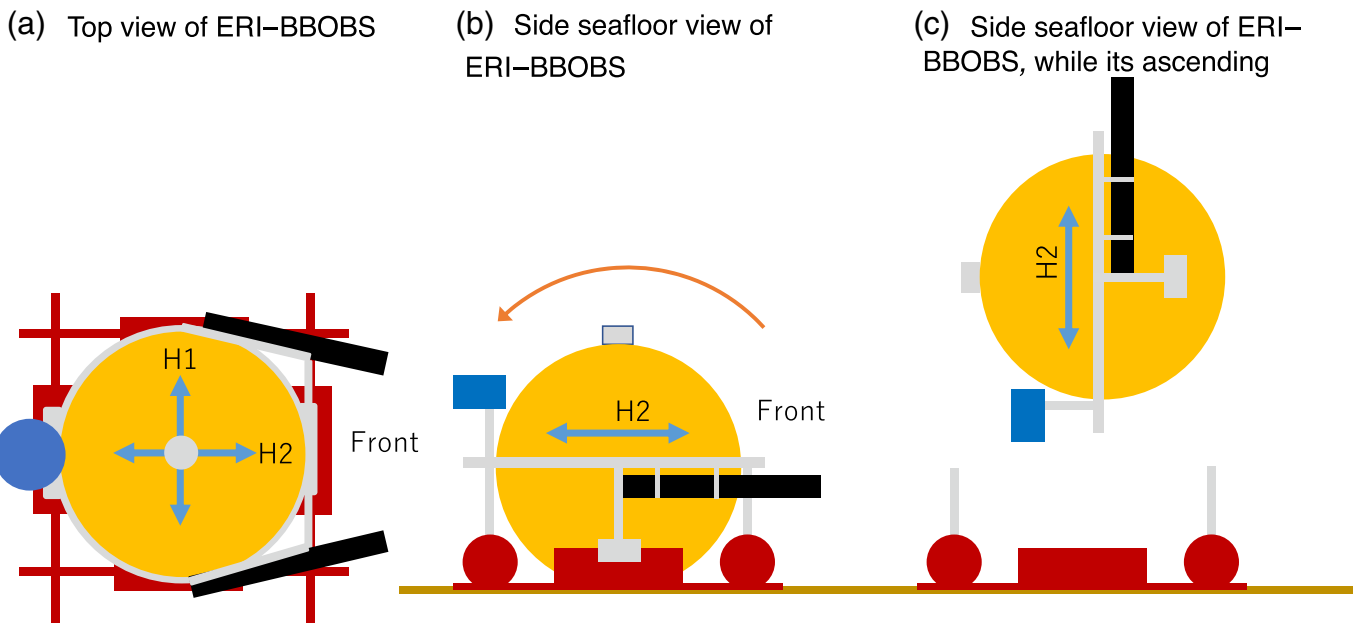
tilt fluctuations are less than $\sim 0.002^\circ$ ($\sim 3.5 \times 10^{-5}$ rad). In the small tilt-fluctuation period, the tilt change estimated from the H2 component has a long-term duration, which is caused by the architecture of the ERI-BBOBS. That is, a torque exists around the H1 axis because the front of the OBS turns up when it ascends (Fig. 12). This long-term duration is observed in most of the stations in the Oldest-1 Array.

By applying arcsine to the admittance of the tilt noise transfer function, we obtained the tilt angle of the vertical component of the sensor. The estimated tilt angles ($-\theta$) were 0.2° – 1.1° , with an average of 0.75° and a median of 0.86° (Table 1). Figure 13 shows the estimated tilt angles and tilt directions (the maximum coherent orientations) relative to the H1 axis. Because the

BBOBSs were deployed by free fall from the sea surface, the maximum coherent orientations are expected to be random and differ among the OBSs. Nevertheless, a bias was obtained in the direction along the H1 axis (Fig. 13). This bias can be understood by considering the architecture of the seismic sensors because CMG-3T requires the three components to be set independently on a common base. The boom of the mass of the vertical component is parallel to the H1 (north-south) axis. Thus, it tends to tilt along the H1 axis, not in the H2 (east-west) axis direction, which is orthogonal to the boom. We suspect that this particular architecture is reflected in the results. The coherent orientation in the off-Miyagi observation shown earlier, which is not along the flow direction, supports this hypothesis. Bell *et al.* (2015) analyzed three types of OBSs and observed the same bias with similar values of θ at the Woods Hole Oceanographic Institution WHOI-Keck BBOBSs also containing CMG-3T sensors. It is worth noting that the other types of OBSs equipped with different seismic sensors (Nanometrics Trillium Compact) did not show bias along the H1 axis.

However, Janiszewski *et al.* (2023) analyzed the noise properties of the U.S. BBOBS from 551 unique stations of 18 U.S.-led deployments, including stations used in Bell *et al.* (2015), and found that the tilt direction is randomly distributed in both BBOBSs equipped with Galperin-type seismometers and WHOI-Keck BBOBSs. This inconsistency suggests that the architecture of the sensor is not the only source controlling the maximum coherent direction.

The CMG-3T sensor of the ERI-BBOBS is stored in a leveling unit that maintains its level within $\pm 0.4^\circ$. The tilt of the leveling unit is recorded once a day during the observation. Therefore, we can directly compare the tilt estimated from the seismograms with the leveling unit outputs. The leveling



unit reports its tilt angles using two independent single-axis tilt meters with 0.1° increments. The tilt angle reported by the leveling unit was stable, except for several days at the beginning of the observation. When the tilt of the leveling unit exceeds the threshold (0.4°), it moves to correct its tilt within the threshold.

The tilt angle change caused by the releveling is detected by both the tilt angles from the admittance and those from the leveling unit, and the amount of change is consistent with each other (Table 1). This consistency suggests that tilt estimation from admittance can be reliable for measuring the tilt of the sensor in ERI-BBOBS. The absolute values of the tilt by the leveling unit and by the admittance, on the other hand, are not consistent. The tilt angle from the admittance was approximately 0.7° larger than that of the leveling unit. The possible causes are (1) remnant tilt in the sensor or leveling unit and/or (2) conversion from input seafloor current to vertical signal as a result of a system response of the ERI-BBOBS, such as asymmetric shape, mass balance, or anchor shape.

CONCLUSIONS

In this study, we modified and tested a procedure to remove tilt and compliance noise from low-frequency vertical-component seismograms recorded by ERI-BBOBSs. Our analysis showed that, unlike those of other types of BBOBSs, the estimated tilt noise transfer functions from the horizontal- to the vertical-component records of the ERI-BBOBSs were stable throughout the observation period. In addition, the transfer functions were frequency independent at frequencies showing a high coherence between the horizontal- and vertical-component seismograms. These results suggest that the transfer function is well described as the tilt of the vertical component from the gravitational direction. Therefore, we applied the tilt noise correction in the time domain. We also removed compliance noise by following the conventional approach. Tilt and compliance

Figure 12. (a) Arrangement of the two horizontal components in an ERI-BBOBS viewed from above. The H2 component is parallel to the front to rear axis. (b,c) The rear is heavier than the front of the BBOBS so that the front rises above the rear during ascension. The color version of this figure is available only in the electronic edition.

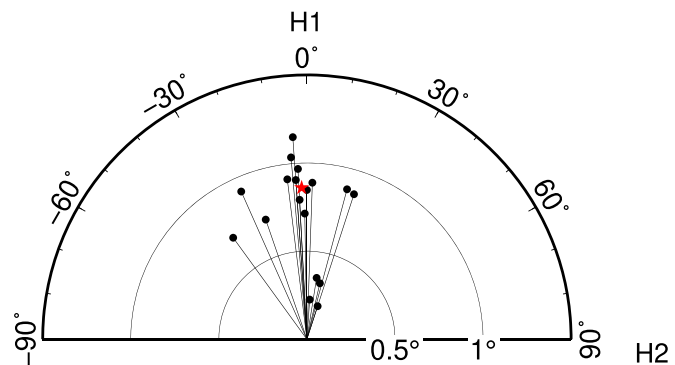


Figure 13. A polar figure of the estimated $-\theta$ and α^{rep} for all BBOBSs deployed in the Oldest-1 Array. The magnitude of $-\theta$ is shown as the diameter of the circle. The α^{rep} are shown as direction of the solid black lines. The number of dots is larger than the number of stations because some stations experienced releveling (readjustment of the horizontal plane of the seismic sensor) during the observation period, which has resulted in a change of the magnitude of θ , so the observation period is divided for stations that have been leveled. Details are shown in Table 1. The red star indicates the median value. The color version of this figure is available only in the electronic edition.

noise-reduced vertical-component spectra showed noise reductions of up to 20 dB at frequencies below ~ 0.03 Hz, allowing us to extract low-frequency (< 0.01 Hz) teleseismic Rayleigh waves.

TABLE 1

Estimated Tilt Angle and Direction of Sensor from Transfer Function and Leveling Unit

Station Name	Periods Until Releveling (yyyy/mm/dd–yyyy/mm/dd)	Tilt Angle Estimated from Admittance (°)	Direction of Tilt from H1 Component (α^{rep})	Tilt Angle along α^{rep} from Leveling Unit (°)*
OL01	2018/10/31–2018/12/12	0.88	15	0.26
	2018/12/13–2019/11/02	0.85	0	0.30
OL02	2018/11/07–2019/10/28	0.97	357	0.40
OL03	2018/11/01–2019/11/03	0.71	359	-0.12
OL04	2018/11/06–2019/08/19	0.79	357	-0.10
	2019/08/20–2019/10/29	0.92	336	-0.09
OL05	2018/11/06–2019/10/28	0.72	341	0.14
OL06	2018/11/03–2019/11/04	0.71	324	-0.11
OL07	2018/11/02–2019/11/01	0.87	18	0.15
OL08	2018/11/05–2019/10/30	1.15	356	0.05
OL09	2018/11/02–2018/11/18	0.23	4	-0.48
	2018/11/19–2019/11/03	0.35	9	-0.35
OL10	2018/11/03–2018/12/16	1.04	355	0.38
	2018/12/17–2019/03/31	0.91	353	0.25
	2019/04/01–2019/07/24	0.89	2	0.23
	2019/07/25–2019/11/04	0.91	356	0.20
OL11	2018/11/04–2018/11/13	0.20	18	-0.41
	2018/11/14–2019/11/03	0.33	13	-0.20

*Tilt angles were calculated from tilt angles measured in 0.1° increments along H1 (north–south) and H2 (east–west) components of the leveling unit. Therefore, the second decimal place is due to the projection.

Finally, we note that the ERI-BBOBS is unique in that it is equipped with a CMG-3T sensor, and thus, the tilt noise reduction demonstrated is applicable to this specific sensor. The estimated maximum tilt directions were along the H1 (north–south) component of the sensor, which can be explained by the architecture of the CMG-3T sensor.

DATA AND RESOURCES

Seismograms and current flow data at offshore Miyagi were collected by the Earthquake Research Institute (ERI), the University of Tokyo, Japan Agency for Marine Science and Technology Center (JAMSTEC), and Kobe University. The seismograms will be released to the public from the Ocean Hemisphere Project Data Management Center (OHPDMC; <http://ohpdmc.eri.u-tokyo.ac.jp>). Seismograms and differential pressure data from the Oldest-1 Array were collected by the ERI and Seoul National University. All data will be released to the public after the priority period ends from the OHPDMC. Mass position output signals and current flow data are available on request from the corresponding author. Some figures were generated using the Generic Mapping Tools (www.soest.hawaii.edu/gmt; Wessel and Smith, 1998). The supplemental figures and table are included in the supplemental material. All websites were last accessed in March 2023.

DECLARATION OF COMPETING INTERESTS

The authors acknowledge that there are no conflicts of interest recorded.

ACKNOWLEDGMENTS

The authors are grateful to the captains and crews of the Research Vessel (R/V) ISABU and R/V ONNURI of Korea Institute of Ocean Science

and Technology (KIOST) for the installation and recovery cruises, respectively. Their efforts led to the success of Oldest-1 Array observation. The authors thank two reviewers and the associated editor for constructive reviews to improve the article. This study was supported by Japan–Korea Basic Scientific Cooperation Program between Japan Society for the Promotion of Science (JSPS) and National Research Foundation of Korea (NRF) (Grant Number JPJSBP120218807) and a Grant-in-Aid for Scientific Research (Grant Number 18H03735) from the JSPS. Y. Kim and S.-M. Lee acknowledge funding from KIOST (Grant Numbers PE99656 and PE99796) and NRF (Grant Number 2022R1A5A1085103).

REFERENCES

- Araki, E., and H. Sugioka (2009). Calibration of deep sea differential pressure gauge, *JAMSTEC Rep. Res. Dev.* **2009**, 141–148, doi: [10.5918/jamstecr.2009.141](https://doi.org/10.5918/jamstecr.2009.141).
- Beauduin, R., and J. P. Montagner (1996). Time evolution of broadband seismic noise during the French pilot experiment OFM/SISMOBS, *Geophys. Res. Lett.* **23**, 2995–2998, doi: [10.1029/96gl02880](https://doi.org/10.1029/96gl02880).
- Bell, S. W., D. W. Forsyth, and Y. Ruan (2015). Removing noise from the vertical component Records of ocean-bottom seismometers: Results from year one of the Cascadia initiative, *Bull. Seismol. Soc. Am.* **105**, 300–313, doi: [10.1785/0120140054](https://doi.org/10.1785/0120140054).
- Crawford, W. C., and S. C. Webb (2000). Identifying and removing tilt noise from low-frequency (<0.1 Hz) seafloor vertical seismic data, *Bull. Seismol. Soc. Am.* **90**, 952–963, doi: [10.1785/0119990121](https://doi.org/10.1785/0119990121).
- Crawford, W. C., S. C. Webb, and J. A. Hildebrand (1991). Seafloor compliance observed by long-period pressure and displacement measurements, *J. Geophys. Res.* **96**, 16,151–16,160, doi: [10.1029/91jb01577](https://doi.org/10.1029/91jb01577).

- Deen, M., E. Wielandt, E. Stutzmann, W. Crawford, G. Barruol, and K. Sigloch (2017). First observation of the earth's permanent free oscillations on ocean bottom seismometers, *Geophys. Res. Lett.* **44**, 10,988–10,996, doi: [10.1002/2017gl074892](https://doi.org/10.1002/2017gl074892).
- Fukao, Y., H. Sugioka, A. Ito, H. Shiobara, J. M. Paros, and R. Furue (2016). Sensing of upslope passages of frontal bores across the trench slope break of the Japan trench, *J. Geophys. Res.* **121**, doi: [10.1002/2015JC011432](https://doi.org/10.1002/2015JC011432).
- Isse, T., D. Suetsugu, A. Ishikawa, H. Shiobara, H. Sugioka, A. Ito, Y. Kawano, K. Yoshizawa, Y. Ishihara, S. Tanaka, et al. (2021). Seismic evidence for a thermochemical mantle plume underplating the lithosphere of the Ontong Java plateau, *Commun. Earth. Environ.* **2**, 98, doi: [10.1038/s43247-021-00169-9](https://doi.org/10.1038/s43247-021-00169-9).
- Janiszewski, H. A., Z. Eilon, J. B. Russell, B. Brunsvik, J. B. Gaherty, S. G. Mosher, W. B. Hawley, and S. Coats (2023). Broad-band ocean bottom seismometer noise properties, *Geophys. J. Int.* **233**, 297–315, doi: [10.1093/gji/ggac450](https://doi.org/10.1093/gji/ggac450).
- Janiszewski, H. A., J. B. Gaherty, G. A. Abers, H. Gao, and Z. C. Eilon (2019). Amphibious surface-wave phase-velocity measurements of the Cascadia subduction zone, *Geophys. J. Int.* **217**, 1929–1948, doi: [10.1093/gji/ggz051](https://doi.org/10.1093/gji/ggz051).
- Kanazawa, T., M. Mochizuki, and H. Shiobara (2001). Broadband seismometer for a long-term observation on the seafloor, *Proc. of the OHP/ION Joint Symposium on Long-Term Observations in the Oceans: Current Status and Perspectives for the Future*, Yamanashi, Japan, 21–27 January 2001, OP-05.
- Lin, P.-Y. P., J. B. Gaherty, G. Jin, J. A. Collins, D. Lizarralde, R. L. Evans, and G. Hirth (2016). High-resolution seismic constraints on flow dynamics in the oceanic asthenosphere, *Nature* **535**, 538–541, doi: [10.1038/nature18012](https://doi.org/10.1038/nature18012).
- Peterson, J. (1993). Observations and modeling of seismic background noise, *U.S. Geol. Surv. Open-File Rept.* 93-322, doi: [10.3133/ofr93322](https://doi.org/10.3133/ofr93322).
- Shiobara, H., A. Ito, H. Sugioka, M. Shinohara, and T. Sato (2021). Tilt observations at the seafloor by mobile ocean bottom seismometers, *Frontiers* doi: [10.3389/feart.2020.599810](https://doi.org/10.3389/feart.2020.599810).
- Shiobara, H., T. Kanazawa, and T. Isse (2013). New step for broad-band seismic observation on the seafloor: BBOBS-NX, *IEEE J. Oceanic Eng.* **38**, no. 2, 396–405, doi: [10.1109/joe.2012.2222792](https://doi.org/10.1109/joe.2012.2222792).
- Suetsugu, D., and H. Shiobara (2014). Broadband ocean-bottom seismology, *Annu. Rev. Earth Planet. Sci.* **42** 27–43, doi: [10.1146/annurev-earth-060313-054818](https://doi.org/10.1146/annurev-earth-060313-054818).
- Tian, Y., and M. H. Ritzwoller (2017). Improving ambient noise cross-correlations in the noisy ocean bottom environment of the Juan de Fuca plate, *Geophys. J. Int.* **210**, 1787–1805, doi: [10.1093/gji/ggx281](https://doi.org/10.1093/gji/ggx281).
- Townsend, B. (2014). Symmetric triaxial seismometers, in *Encyclopedia of Earthquake Engineering*, M. Beer, I. A. Kougioumtzoglou, E. Patelli, and S.-K. Au (Editors), Springer, Berlin, Heidelberg, 1–19, doi: [10.1007/978-3-642-35344-4_194](https://doi.org/10.1007/978-3-642-35344-4_194).
- Usher, M. J., C. Guralp, and R. F. Burch (1978). The design of miniature wideband seismometers, *Geophys. J. Int.* **55**, no. 3, 605–613, doi: [10.1111/j.1365-246x.1978.tb05930.x](https://doi.org/10.1111/j.1365-246x.1978.tb05930.x).
- Webb, S.C., T. K. Deaton, and J. C. Lemire (2001). A broadband ocean-bottom seismometer system based on a 1-Hz natural period geophone, *Bull. Seismol. Soc. Am.* **91**, 304–312, doi: [10.1785/0120000110](https://doi.org/10.1785/0120000110).
- Wessel, P., and W. H. F. Smith (1998). New, improved version of Generic Mapping Tools released, *Eos Trans. AGU* **79**, no. 47, 579.
- Yang, X., Y. Luo, H. Xu, and K. Zhao (2020). Shear wave velocity and radial anisotropy structures beneath the central Pacific from surface wave analysis of OBS records, *Earth Planet. Sci. Lett.* **534**, 116,086, doi: [10.1016/j.epsl.2020.116086](https://doi.org/10.1016/j.epsl.2020.116086).

APPENDIX

Coherence between the horizontal- and vertical-component seismograms

To illustrate the coherent relationship between the horizontal- and vertical-component seismograms, we first divide the 24 hr time series into 2000 s sections with a 50% overlap between adjacent sections and discard any sections containing glitches and earthquake-generated signals. Using the remnant noise sections, we calculate the daily cross and power spectra of noise as

$$G_{HZ}(f) = \frac{1}{n_d} \sum_{i=1}^{n_d} H_i^*(f) Z_i(f), \quad (A1)$$

$$G_{HH}(f) = \frac{1}{n_d} \sum_{i=1}^{n_d} H_i^*(f) H_i(f), \quad (A2)$$

$$G_{ZZ}(f) = \frac{1}{n_d} \sum_{i=1}^{n_d} Z_i^*(f) Z_i(f), \quad (A3)$$

in which n_d is the number of 2000-s-long noise sections included in a 24 hr time series, and $H_i(f)$ and $Z_i(f)$ are the Fourier-transformed horizontal- and vertical-component seismograms of the i th section, respectively. The squared coherence between the horizontal and vertical components on day d is given by

$$\gamma_d^2(f) = \frac{|G_{HZ}(f)|^2}{G_{HH}(f)G_{ZZ}(f)}. \quad (A4)$$

We rotate the horizontal component to find the direction of horizontal displacement with the maximum square coherence with the vertical similar to Bell et al. (2015). The maximum coherent orientation, which maximizes the squared coherence (equation A4) averaged over a frequency range of 0.02–0.06 Hz, is searched by rotating and composing the two horizontal components at a 1° interval clockwise from H1 component axis (north–south component of the sensor). The definitions of uncertainties for each variable follow Bell et al. (2015).

Manuscript received 15 December 2022

Published online 18 April 2023